



Optimization and application of the distribution of relaxation times based on characteristic frequency resolution and hyperparameters

Dong Zhu, Tiancai Ma ^{*}, Yanbo Yang ^{**}

School of Automotive Studies, Tongji University, Shanghai, 201804, China

HIGHLIGHTS

- DRT based on characteristic frequency resolution and hyperparameter is proposed.
- Characteristic frequency resolution optimization can overcome peaks overlapping.
- Hyperparameter optimization is applied to improve the robustness of DRT.
- Fast EIS measurement based on characteristic frequency of DRT is investigated.

ARTICLE INFO

Keywords:

Distribution of relaxation times
Electrochemical impedance spectroscopy
Characteristic frequency resolution
Hyperparameters optimization
Proton exchange membrane fuel cell

ABSTRACT

Distribution of relaxation times (DRT) is a promising method for interpreting electrochemical impedance spectroscopy (EIS) data. Contemporary studies have made significant progress in theory, algorithm, implementation, and application of DRT. However, the DRT deconvolution is often difficult to interpret because of the pseudo-peaks, peaks deviation or peaks overlapping. In this paper, a comprehensive regularization DRT method based on characteristic frequency resolution and hyperparameters is proposed. Based on quantitative analysis of synthetic simulation data, the characteristic frequency resolution optimization is applied to avoid the peaks overlapping and improve the accuracy of DRT. Meanwhile, the hyperparameters optimization which assigns weights to each individual data point is verified to improve the robustness of DRT. Then, the optimized DRT is applied to the EIS experimental data analysis of proton exchange membrane fuel cell (PEMFC), and the polarization processes of PEMFC are identified. Moreover, a fast EIS measurement based on characteristic frequency of DRT is proposed and verified by the impedance prediction which the deviations are within 10%, but the EIS measurement time is shortened from 6 min to 5 s. Moreover, this method can provide a new direction and idea for fault diagnosis based on EIS data, especially for on-board applications.

1. Introduction

Electrochemical impedance spectroscopy (EIS) has become an attractive electrochemical characterization technology for scientific research, for example, fuel cells [1–4], solar cells [5,6], lithium-ion batteries [7–9], and biomedical applications [10]. Electrochemical or physical processes which contain transport, kinetic, thermal processes occurring at different relaxation times can be obtained by EIS [11,12]. The typical analysis method used to interpret the obtained EIS data is the equivalent circuit model (ECMs). However, the ECMs method requires prior knowledge and has an ambiguity problem in which multiple ECMs

can fit the same data well [13,14]. While gene expression programming [15] and neural networks [16] can be used to automatically search for ECMs, physically interpreting and ascertaining their uniqueness remains a challenge. As suggested by Macdonald [17], most ECMs are merely representative of the data, not to identify and interpret the physico-chemical parameters and processes involved.

To solve the above problems, the distribution of relaxation times (DRT) is a complementary method that can analyze the EIS data. DRT, as a model-free method of quasi-infinite series of R//C elements that can identify the relaxation times and characteristic frequencies of the electrochemical system with no need for prior knowledge, has been

* Corresponding author.

** Corresponding author.

E-mail addresses: matiancai@tongji.edu.cn (T. Ma), yanboyang@tongji.edu.cn (Y. Yang).

attracting more and more attention. However, the solving procedure of DRT exists ill-posed and over-fitting problems [18]. In this regard, various methods have been proposed, including regularization method [19,20], Monte Carlo method [21], Fourier transforms [22], maximum entropy [23], and so on. The regularization method has become the mainstream of research because of its advantages in simple operation and adjustable noise resistance [24]. T. Ivers et al. [24] made an in-depth summary of the basic theory, regularization methods, and diagnostic applications of DRT. K. Kobayashi et al. [25] focused on discussing continuous relaxation time distribution and discrete relaxation time distribution of DRT. Ciucci et al. [26] conducted many theoretical studies on regularization DRT based on the Bayesian framework and the hyperparameters method had been proposed for the detection of discontinuities in the DRT and the outliers in EIS data. The DRT has been applied to analyze the aging state of solid oxide fuel cells [1,27] and lithium-ion batteries [28,29] because of the excellent analytical ability in interpreting the individual polarization process. In proton exchange membrane fuel cell (PEMFC), DRT is mainly used to qualitatively analyze the relationship between the peaks of different time constants and electrochemical polarization processes [11,30,31].

Although numerical regularization DRT has made significant progress in theory, algorithm, implementation, and application, the DRT deconvolution may confuse the interpretation of the electrochemical system because of the pseudo-peaks, peaks deviation, and peaks overlapping [24]. The numerical regularization DRT has several important input parameters, such as the frequency range of the DRT, points per decade (ppd) of EIS data, impedance value, number of radial basis functions (RBFs), and regularization parameter λ [32,33]. At present, most studies focus on improving the analysis accuracy of DRT by optimizing λ . However, regularization parameter optimization only plays a role in avoiding pseudo-peaks caused by noise but has little effect on peaks overlapping [32]. Moreover, the hyperparameters approach shows great power in eliminating pseudo-peaks and detection of outliers in EIS data, but is also incapable of peak overlapping. Unfortunately, the number of RBFs is often overlooked, it affects a significant indicator in DRT analysis: the characteristic frequency resolution, which represents the ability to separate two adjacent relaxation times. Furthermore, one of the main bottlenecks in the application of EIS for fault diagnosis is the long measurement time which takes a few minutes to scan the entire spectrum [34]. To solve this problem, various multi-frequency test methods have been proposed to shorten the EIS measurement time [35–37]. But the precision of EIS measurement and polarization processes identification are the mainly limiting factors.

In this paper, a comprehensive regularization DRT based on characteristic frequency resolution and hyperparameters method is proposed to overcome peaks overlapping, pseudo-peaks and peaks deviation. First, the principle of characteristic frequency resolution is discussed in detail, and the influence of characteristic frequency resolution on overlapping peaks and the identification accuracy of time constant is analyzed through synthetic experiments. Then, to improve the robustness of DRT, the hyperparameters method is applied to correct the peaks deviation and the pseudo-peaks caused by erroneous points or noise. Second, the improved DRT approach is applied to interpret the EIS data of PEMFC, and the specific DRT peak is compared with the theoretical charge transfer resistance model to verify the effectiveness of this method. Finally, the criteria of frequency range selection based on characteristic frequency of DRT peak for fast EIS measurement is proposed and verified by impedance prediction.

2. Experimental setups

2.1. PEMFC assembly

The commercial membrane electrode assembly (MEA) produced by Hyplat is shown in Fig. S1(a) of supporting information. The active surface area the MEA is 25 cm². The MEA is manufactured by catalyst

Table 1

The operation conditions of the polarization curve.

Parameters	Values
Current density range (mA cm ⁻²)	150–1500
Cell temperature (°C)	60
Inlet gas temperature (°C)	60
Inlet gas relative humidity (%)	100
Hydrogen mass flow (mL min ⁻¹)	500
Air mass flow (mL min ⁻¹)	2000
Anode back pressure (bar)	0
Cathode back pressure (bar)	0

coated membrane (CCM) process with platinum (Pt) loadings of 0.4 mg cm⁻² and 0.1 mg cm⁻² in the cathode and anode, respectively, and with commercial proton exchange membrane (PEM) of 15 μm. The PEMFC assembly (Scriber QCF25) comprises graphite bipolar plates with single serpentine flow fields, stainless steel endplates with heater strips, and temperature sensors.

2.2. Experimental equipment

Impedance measurement equipment consists of fuel cell testbench (Hephas PEMTest50), electrochemical workstation (Metrohm Autolab PGSTAT 302 N), programmable electronic load (Kikusui PLZ664WA), dynamic load interface (Dynload interface), and controlling software of NOVA (Fig. S1(b) in supporting information).

2.3. Experimental procedure

Before the EIS test, the PEMFC is operated at 800 mA cm⁻² under fully humidified conditions for more than 1 h to activate and ensure fully hydrated. The polarization curve is measured in the galvanostatic mode for 5 min to get to equilibrium. Table 1 shows the operating conditions of the polarization curve. At the end time of each DC point of polarization curve, an impedance spectrum of sinusoidal AC is applied and set to 6% of the DC load [38]. The frequency range is from 10 kHz to 0.1 Hz with 11 ppd.

3. Improved DRT method

3.1. Distribution of relaxation times

In an electrochemical system, the relaxation time is the time required to characterize a certain electrochemical process from transient to stable. The DRT method can extract the electrochemical relaxation times from EIS by deconvolution. The relationship between the complex impedance $Z(f)$ and the distribution function of relaxation times $g(\tau)$ is as follow:

$$Z(f) = R_0 + Z_{\text{pol}}(f) = R_0 + R_{\text{pol}} \int_0^{\infty} \frac{g(\tau)}{1 + j2\pi f\tau} d\tau \quad (1)$$

where τ is the time constant of the R//C element depicted by $\tau = RC = 1/f_r$, f_r is the frequency of corresponding time constant (The radian frequency is used instead of the frequency for ease of calculation). R_0 represents the ohmic resistance, $Z_{\text{pol}}(f)$ is the polarization impedance, R_{pol} is the polarization resistance. The EIS data are usually taken into the logarithmic scale, and the Equation (5) can be written to the below:

$$Z(f) = R_0 + Z_{\text{pol}}(f) = R_0 + R_{\text{pol}} \int_{-\infty}^{\infty} \frac{\gamma(\ln\tau)}{1 + j2\pi f\tau} d(\ln\tau) \quad (2)$$

where $\gamma(\ln\tau) = \tau g(\tau)$.

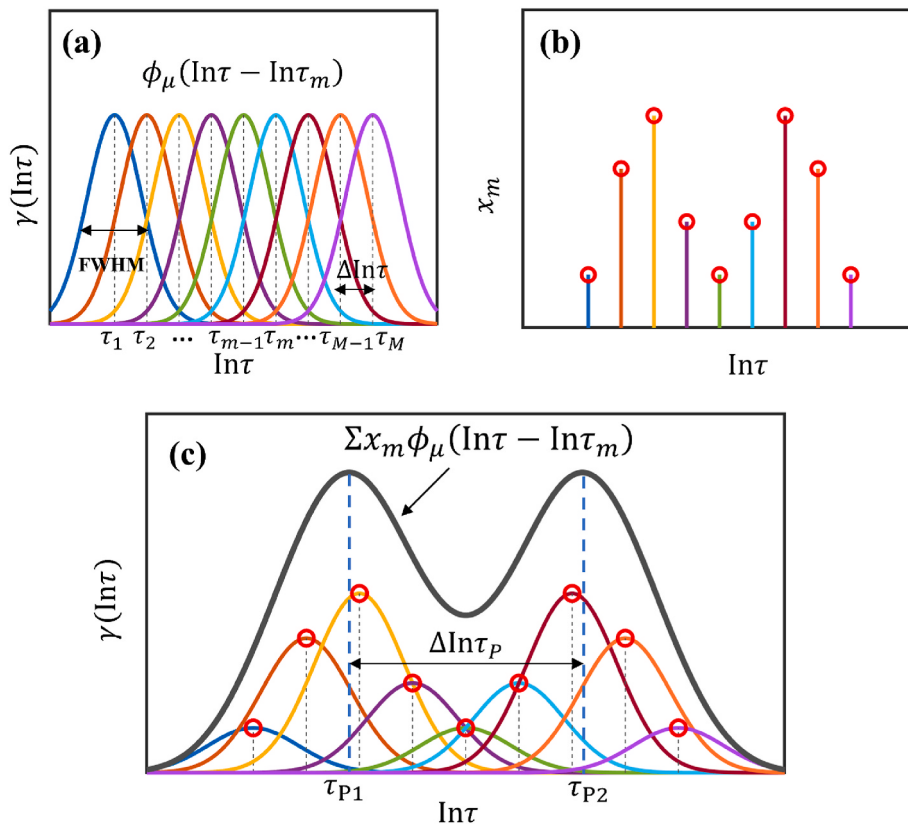


Fig. 1. Schematic of the RBF-based numerical DRT, (a) RBFs, (b) x_m , (c) $\gamma(\text{Int}\tau)$.

3.2. Characteristic frequency resolution of numerical DRT

In analyzing the EIS of PEMFCs, a series of common equivalent circuit elements are used to represent physically meaningful polarization processes of transport and reaction in porous electrodes [3]. Common equivalent circuit elements include RQ (parallel the resistance R and constant phase element Q), Gerischer and Warburg elements. The impedance of these elements can be obtained by the analytical DRT [1, 39]. For example, the analytical DRT of an RQ element is as follows [1]:

$$g(\tau) = \frac{R_{\text{pol}}}{2\pi\tau} \frac{\sin((1-n_Q)\pi)}{\cosh(n_Q(\ln(\tau/\tau_{\text{RQ}}))) - \cos((1-n_Q)\pi)} \quad (3)$$

where n_Q is the coefficient of constant phase element, τ_{RQ} is the characteristic time constant of RQ element. When the $n_Q = 1$, the RQ element degenerates into an ideal RC element. And the analytical DRT is Dirac-pulse and located at its characteristic frequency. But the analytical DRT is not applied for the discrete EIS data. So, a large number of numerical DRT methods have emerged [18, 19, 24, 40]. However, most of them do not consider the resolution of relaxation times in numerical DRT deconvolution and its influencing factors. In the next, we will discuss this concept and propose an improved numerical DRT approach.

Discretization is the critical procedure of numerical DRT. From the above analysis, the Z_{DRT} is usually discretized by Voigt circuits [41]. This discretization can be thought of as the sum of Dirac distributions $\delta(\text{Int}\tau)$ with time constant $\tau_1, \tau_2, \dots, \tau_m, \dots, \tau_M$.

$$\gamma(\text{Int}\tau) = \sum_{m=1}^M x_m \delta(\text{Int}\tau - \text{Int}\tau_m) \quad (4)$$

where x_m is the coefficient of Dirac distributions. Since the DRT distribution of most electrochemical systems is continuous, but the Dirac distribution will lead to the discontinuity of DRT distribution, the discretization of DRT needs to be represented by the sum of continuous

distributions. Then, the approximated $\gamma(\text{Int}\tau)$ can be written as follow:

$$\gamma(\text{Int}\tau) = \sum_{m=1}^M x_m \phi_\mu(\text{Int}\tau - \text{Int}\tau_m) \quad (5)$$

where $\phi_\mu(\text{Int}\tau - \text{Int}\tau_m)$ is an RBF with center time constant τ_m and shape parameter μ . Fig. 1 shows the schematic of the RBF-based numerical DRT. A lot of RBFs can be used for the discretization of DRT. Because of the positive definiteness and differentiability [20], the Gaussian functions ($\phi_\mu(x) = \exp(-(\mu x)^2)$) are chosen as RBFs in this work and shown in Fig. 1 (a). The RBF shape parameter μ determines the full width at half maximum (FWHM) for the discretized RBFs. If μ is large, it will oscillate near each time constant point. On the other hand, if μ is small, the numerical DRT will be flattened [33]. Hence, in this work the FWHM is twice as much as the time constant resolution $\Delta\text{Int}\tau$ and the corresponding formula is as follow.

$$\text{FWHM} = 2\Delta\text{Int}\tau = \frac{1.665}{\mu} \quad (\text{Gaussian function}) \quad (6)$$

$$\Delta\text{Int}\tau = \frac{\text{Int}\tau_M - \text{Int}\tau_1}{M-1} = -\frac{1}{2.303} \Delta\log f \quad (7)$$

The time constant resolution $\Delta\text{Int}\tau$ is affected by the time constant range and the selection of the number of M . Most of the time, the time constant range is related to the frequency measurement range. If the frequency measurement range of EIS data is determined, the number of M is the critical parameter affecting the $\Delta\text{Int}\tau$. x_m which can be obtained by regularization method is shown in Fig. 1(b). Fig. 1(c) shows the approximated $\gamma(\text{Int}\tau)$ using Equation (5) which is the sum of RBFs multiply by x_m . The logarithmic interval between the two DRT peaks is $\Delta\text{Int}\tau_P$. Obviously, with the increase of the $\Delta\text{Int}\tau$, the number of RBFs decreases. When the $\Delta\text{Int}\tau$ is larger than the $\Delta\text{Int}\tau_P$, the approximated $\gamma(\text{Int}\tau)$ is consist of only one RBF, so, the DRT peaks must be only one. If

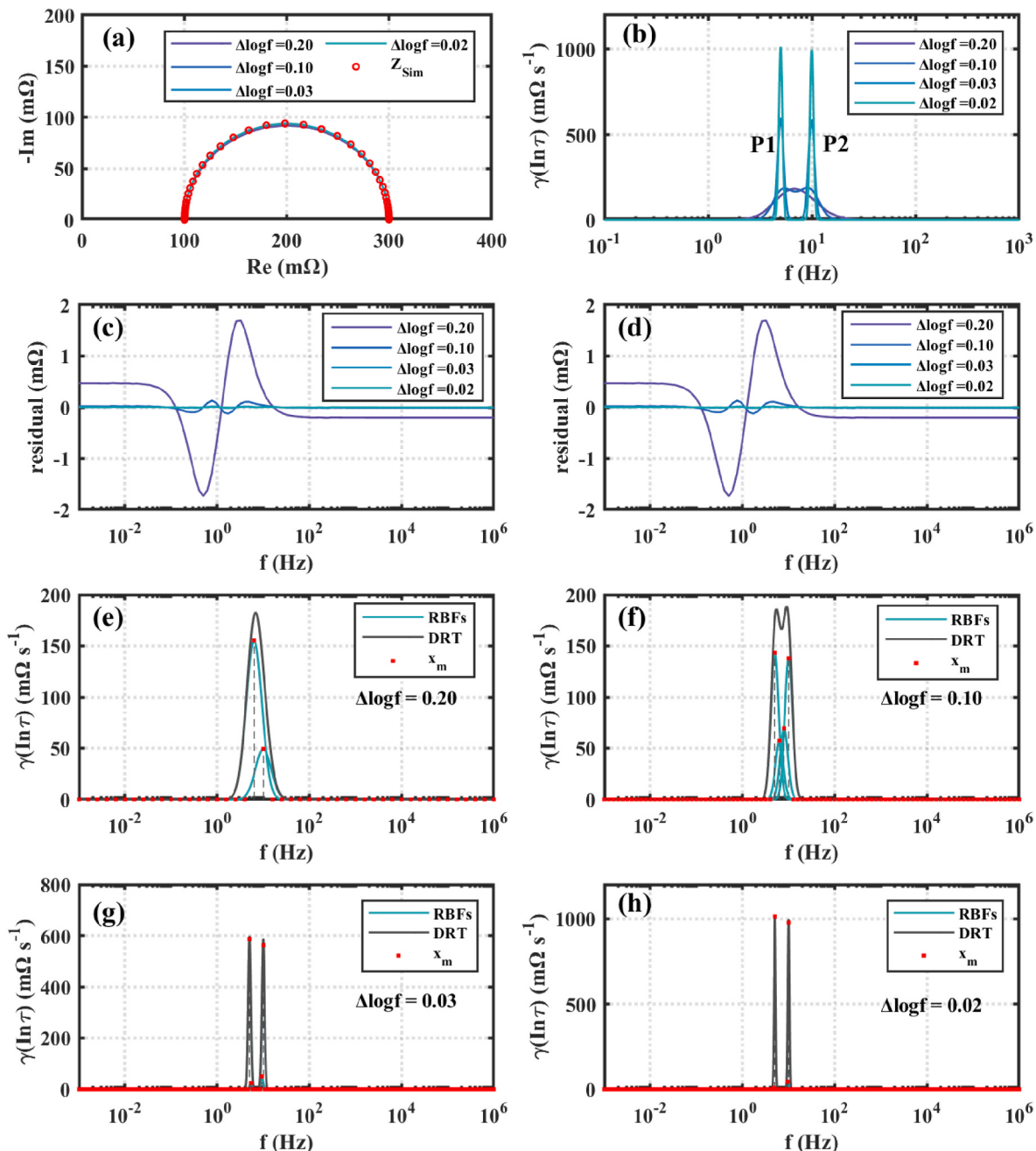


Fig. 2. The numerical DRT results with different $\Delta\log f$ at $\lambda = 1e-12$, (a) Nyquist plots, (b) DRT plots, (c) residual of real part vs. frequency, (d) residual of imaginary part vs. frequency, (e) RBFs and x_m of $\Delta\log f = 0.20$, (f) RBFs and x_m of $\Delta\log f = 0.10$, (g) RBFs and x_m of $\Delta\log f = 0.03$, (h) RBFs and x_m of $\Delta\log f = 0.02$.

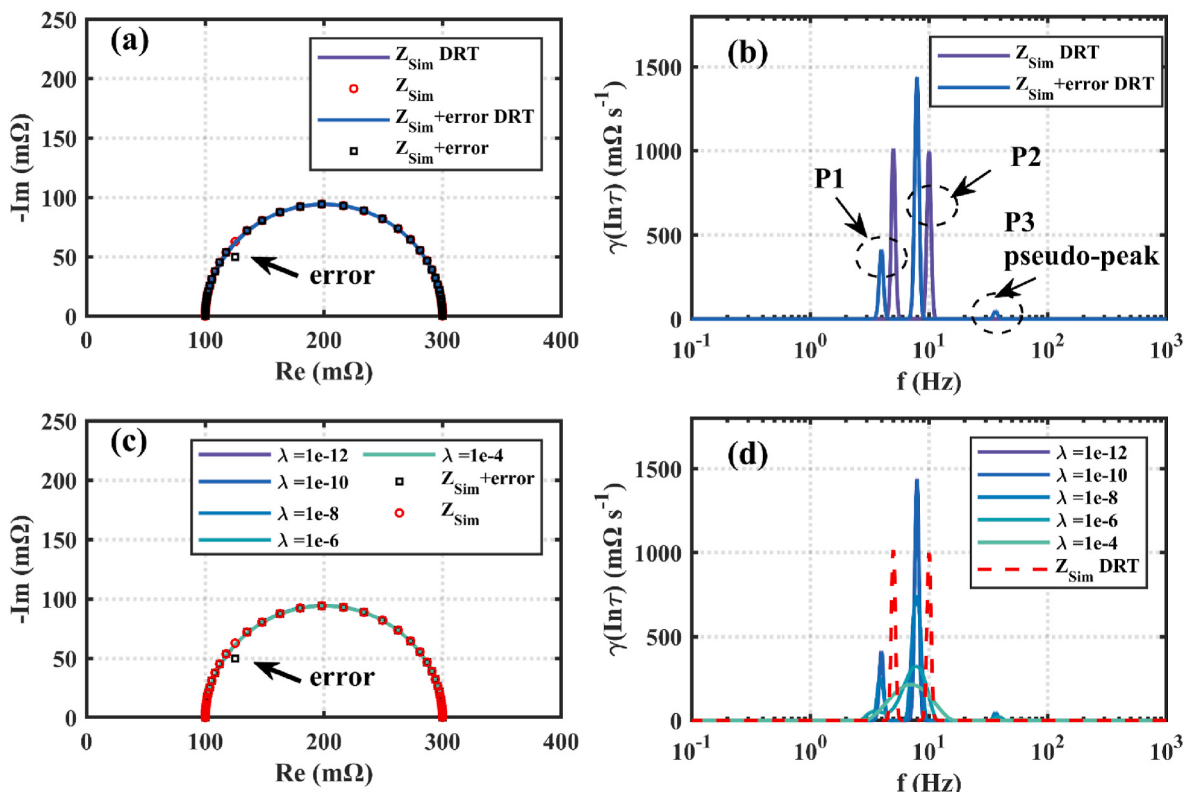
the logarithmic interval between the two characteristic relaxation times of an electrochemical system is less than the $\Delta\ln\tau$, the characteristic relaxation times may not be resolved. For better calculation and comparison, the characteristic frequency resolution $\Delta\log f$ which is represented in logarithmic form based on 10 is used for the DRT analysis and takes the positive value.

To verify the influence of $\Delta\log f$ on numerical DRT, the synthetic EIS data of Randles circuit ($\tau_{R_1C_1} = 2\tau_{R_2C_2} = 0.2$ s, $R_1 = R_2 = R_3 = 100$ mΩ) is analyzed. Fig. S2(a) in supporting information shows the detail information. The characteristic frequencies of $f_{R_1C_1}$ and $f_{R_2C_2}$ are 5 Hz and 10 Hz and the logarithmic frequency interval $\Delta\log f_{RC}$ is 0.3. Four different $\Delta\log f$ are used for the numerical DRT from 0.02 to 0.2. Fig. 2(a) and (b) show the fitted Nyquist plots and the DRT plots with different

$\Delta\log f$ at $\lambda = 1e-12$. The fitted Nyquist plots gradually deviate from the original data Z_{sim} with the increase of $\Delta\log f$ in the middle and low frequency range (0.1–10 Hz). This tendency can be seen more clearly from the residuals plots in Fig. 2(c) and (d). The amplitude of oscillation increases rapidly from 0.1–10 Hz with the increase of $\Delta\log f$. Even though the maximum residuals are less than 1%. However, $\Delta\log f$ has a much greater effect on numerical DRT. From Fig. 2(b), with the increase of $\Delta\log f$, the characteristic frequency resolution reduces, the DRT peaks become flat gradually. When $\Delta\log f$ is 0.2 which is larger than $\Delta\log f_{RC}/2$, the DRT peaks degenerate from two to one, that means the time constant of the Randles circuit is unable to identify. This is very similar to the frequency resolution in the Discrete Fourier Transform (DFT), $\Delta\log f$ represents the ability to separate two adjacent relaxation times. From

Table 2The fitting accuracy of numerical DRT at different $\Delta \log f$.

Parameters		$\Delta \log f = 0.02$	$\Delta \log f = 0.03$	$\Delta \log f = 0.1$	$\Delta \log f = 0.2$
P1	Characteristic frequency (Hz)	Value	9.98	9.96	9.004
		Residual	0.253%	0.42%	9.96%
	Time constant (s)	Value	0.1003	0.1004	0.111
		Residual	0.3%	0.4%	11%
P2	Peak area (mΩ)	Value	100.001	100.124	102.24
		Residual	0.001%	0.124%	2.24%
	Characteristic frequency (Hz)	Value	5.022	5.028	5.423
		Residual	0.44%	0.56%	8.46%
P2	Time constant (s)	Value	0.1991	0.1989	0.184
		Residual	0.45%	0.55%	8%
	Peak area (mΩ)	Value	99.9998	99.88	97.79
		Residual	0.0002%	0.11%	2.21%

**Fig. 3.** The numerical DRT of EIS data of $Z_{\text{sim}} + \text{error}$, (a) Nyquist plots with or without one erroneous point, (b) corresponding DRT plots, (c) Nyquist plots with different λ from $1e-4$ to $1e-12$, (d) corresponding DRT plots.

the above analysis, when $\Delta \log f$ is greater than half of the $\Delta \log f_{\text{RC}}$, the numerical DRT method cannot distinguish the time constants. Fig. 2(e)–(f) shows the RBFs and the coefficient x_m of numerical DRT with different $\Delta \log f$. From Fig. 2(e), due to the large $\Delta \log f$, there are only two RBFs in $\Delta \log f_{\text{RC}}$. The DRT has only one peak. When $\Delta \log f = \Delta \log f_{\text{RC}}/3 = 0.1$ in Fig. 2(f), two peaks start to appear but do not separate. With the further decrease of $\Delta \log f$, the two peaks gradually separate completely in Fig. 2(g) and (h). Table 2 shows the fitting accuracy of numerical DRT at different $\Delta \log f$. With the decrease of $\Delta \log f$, the time constants and resistance (obtained by peaks areas) of DRT peaks get closer to those of the theoretical Randles circuit and the characteristic frequency resolution of DRT increases. In the following, $\Delta \log f$ is set to 0.02 unless otherwise specified.

3.3. Robustness of the numerical DRT

The above analysis is based on ideal synthetic EIS data. For actual measurement data, measurement error or noise caused by measuring equipment or testing process may be included [42]. Therefore, the robustness of numerical DRT to error or noise is the critical factor for the application.

Firstly, one erroneous point at 3 Hz which interferes with the surrounding peaks is added to the Z_{sim} of above Randle circuit. Fig. 3 shows the comparison of the numerical DRT results of Z_{sim} with or without one erroneous point at λ equals $1e-12$. Although the Nyquist plots in Fig. 3(a) fitted by the $Z_{\text{sim}} + \text{error}$ is almost consistent with Z_{sim} , the impact of one erroneous point on the DRT peaks in Fig. 3(b) is significant. The characteristic frequencies of DRT peaks are shifted, and the area of DRT

Table 3The fitting accuracy of numerical DRT with or without hyper- ϵ ($Z_{\text{sim}} + \text{error}$).

Parameters		Z_{sim}	$Z_{\text{sim}} + \text{error}$	$Z_{\text{sim}} + \text{error}$ hy- ϵ
P1	Characteristic frequency (Hz)	Value	9.9747	7.923
	Residual	0.253%	20.7%	6.4%
	Time constant (s)	Value	0.1003	0.126
	Residual	0.3%	26%	6%
P2	Peak area (mΩ)	Value	100.001	152.6
	Residual	0.001%	52.6%	3.85%
	Characteristic frequency (Hz)	Value	5.022	3.97
	Residual	0.44%	20.6%	4%
P3	Time constant (s)	Value	0.1991	0.252
	Residual	0.45%	26%	4.5%
	Peak area (mΩ)	Value	99.9998	42.54
	Residual	0.0002%	57.46%	3.2%
P3	Characteristic frequency (Hz)	Value	\	36.23
	Residual	\	\	\
	Time constant (s)	Value	\	0.028
	Residual	\	\	\
P3	Peak area (mΩ)	Value	\	4.85
	Residual	\	\	\

peaks is obviously unbalanced, although the sum of the two DRT peaks area changes a little from Table 3. Moreover, a pseudo-peak appears caused by the erroneous point.

The above results indicate that the numerical DRT method is very sensitive to the quality of impedance data. In most of the current studies, the method of adjusting regularization parameter λ is usually used to optimize the fitting results of DRT. The optimization of λ is often used to suppress artifacts [11,24,30]. Meanwhile, algorithms for automatically optimizing regularization parameters have been proposed, including the cross-validation method [43], the discrepancy method [18], the L-curve

criterion [44], and so on.

Fig. 3(c) and (d) shows the numerical DRT results with different λ from 1e-4 to 1e-12 of the $Z_{\text{sim}} + \text{error}$. Although the Nyquist plots in Fig. 3(c) fitted by the numerical DRT with different λ are almost unanimous, but the shape of DRT peaks flattens out as the λ increases in Fig. 3(d). The additional pseudo-peak caused by erroneous point is suppressed, but the deviation of DRT peaks is not improved with the increase of λ . Worse, at $\lambda = 1\text{e-}4$, the DRT peaks are reduced to one. From the above analysis, the optimization of λ can suppress the pseudo-peaks but not much improvement on the maladjusted DRT peaks.

In order to improve the robustness of the numerical DRT, this paper combines the hyperparameters of the hierachal Bayesian DRT [26,33], which can assign weights to each data point to detect outliers in EIS data. In the Bayesian framework, the weight vector of the residuals of impedance real part ϵ_{re} and the residuals of impedance real part ϵ_{im} can be assumed to random variables with priors of their own. These hyperparameters have probability distribution functions (PDFs) which is denoted as $p_{\text{HP}}(\epsilon_{\text{re}})$ and $p_{\text{HP}}(\epsilon_{\text{im}})$. Due to the excellent tunability of Gamma distribution, it is selected as the initial value of the hyperparameters [33]. So, the distribution can be written as follow:

$$p_{\text{HP}}(\epsilon_{\text{re}}) \propto \epsilon_{\text{re}}^{\frac{\beta}{2}-1} \exp\left(-\frac{\zeta}{2}\epsilon_{\text{re}}\right) \quad (8a)$$

$$p_{\text{HP}}(\epsilon_{\text{im}}) \propto \epsilon_{\text{im}}^{\frac{\beta}{2}-1} \exp\left(-\frac{\zeta}{2}\epsilon_{\text{im}}\right) \quad (8b)$$

where $\beta/2$ is the shape parameter, $\zeta/2$ is the reciprocal of scale parameter. By using the hyperparameters of ϵ_{re} and ϵ_{im} (called hyper- ϵ), the PDFs of the posterior probability $p(x, \epsilon_{\text{re}}, \epsilon_{\text{im}} | Z_{\text{exp},\text{re}}, Z_{\text{exp},\text{im}})$ can be expressed as:

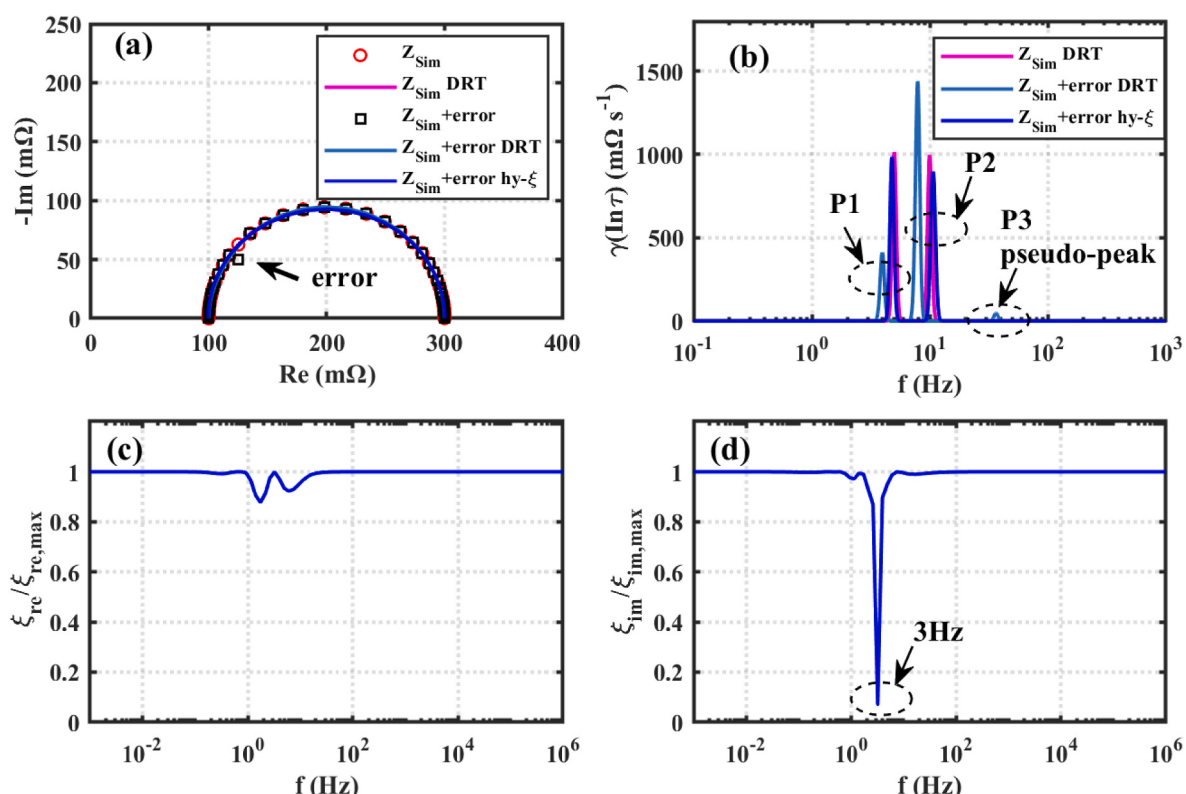


Fig. 4. The numerical DRT results of EIS data of $Z_{\text{sim}} + \text{error}$ with or without hyper- ϵ ($\beta' = \beta'' = 2$, $\zeta' = \zeta'' = 10$), (a) Nyquist plots, (b) DRT plots, (c) the normalized weights of the real parts, (d) the normalized weights of the imaginary parts.

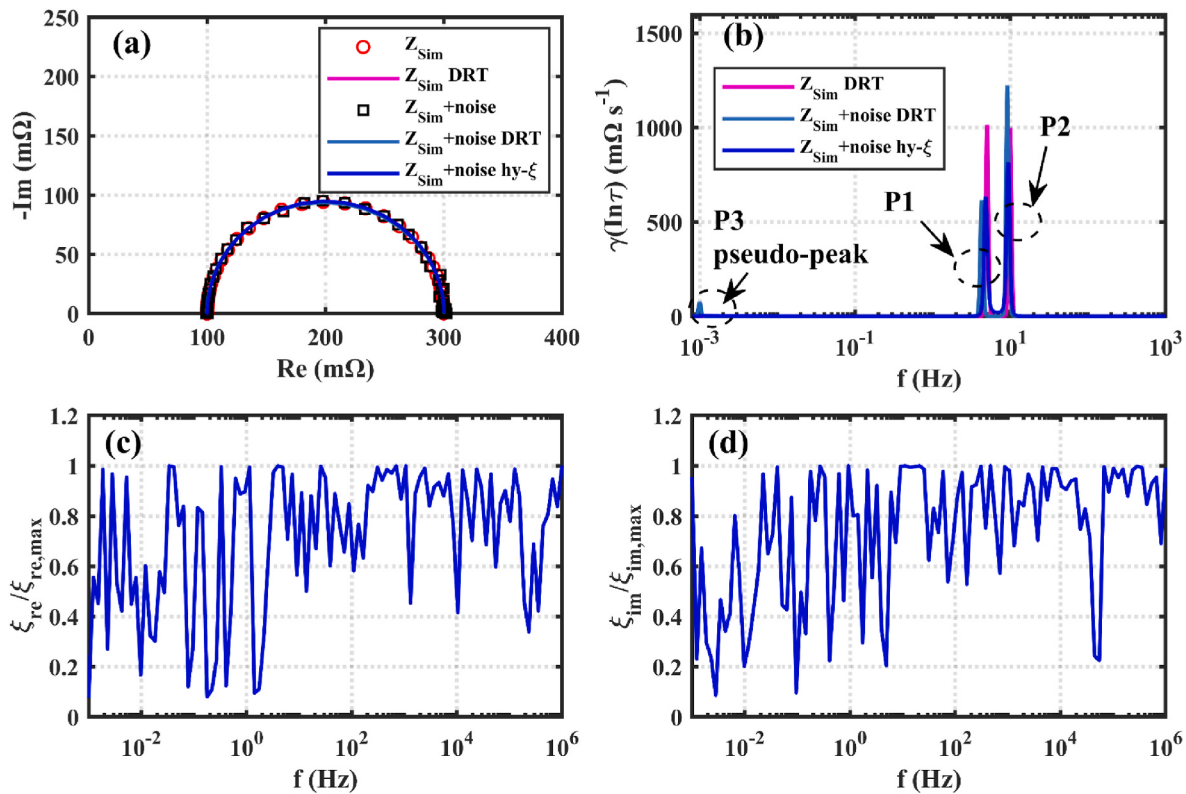


Fig. 5. The numerical DRT results of $Z_{\text{sim}} + \text{noise}$ with or without hyper- ϵ ($\beta' = \beta'' = 2$, $\zeta' = \zeta'' = 10$), (a) Nyquist plots, (b) DRT plots, (c) the normalized weights of the real parts, (d) the normalized weights of the imaginary parts.

$$p(\mathbf{x}, \boldsymbol{\varepsilon}_{\text{re}}, \boldsymbol{\varepsilon}_{\text{im}} | \mathbf{Z}_{\text{exp,re}}, \mathbf{Z}_{\text{exp,im}}) \propto \exp \left(-\frac{1}{2} \mathcal{L}_{\text{ridge}}^{\text{hyper}}(\mathbf{x}, \boldsymbol{\varepsilon}_{\text{re}}, \boldsymbol{\varepsilon}_{\text{im}}) \right) \propto \prod_{m=1}^M \sqrt{\varepsilon_{\text{re},m}} \sqrt{\varepsilon_{\text{im},m}} \exp \left(-\frac{1}{2} \sum_{m=1}^M \varepsilon_{\text{re},m} E_{\text{re},m^2} - \frac{1}{2} \sum_{m=1}^M \varepsilon_{\text{im},m} E_{\text{im},m^2} - \frac{\lambda}{2} \mathbf{L} \mathbf{x}^2 + \sum_{m=1}^M \left(\left(\frac{\beta'}{2} - 1 \right) \ln \varepsilon_{\text{re},m} - \frac{\zeta'}{2} \varepsilon_{\text{re},m} \right) + \sum_{m=1}^M \left(\left(\frac{\beta''}{2} - 1 \right) \ln \varepsilon_{\text{im},m} - \frac{\zeta''}{2} \varepsilon_{\text{im},m} \right) \right) \quad (9)$$

where

$$\mathcal{L}_{\text{ridge}}^{\text{hyper}}(\mathbf{x}, \boldsymbol{\varepsilon}_{\text{re}}, \boldsymbol{\varepsilon}_{\text{im}}) = \sum_{m=1}^M \varepsilon_{\text{re},m} E_{\text{re},m^2} + \sum_{m=1}^M \varepsilon_{\text{im},m} E_{\text{im},m^2} - (\beta' - 1) \ln \varepsilon_{\text{re},m} + \zeta' \varepsilon_{\text{re},m} - (\beta'' - 1) \ln \varepsilon_{\text{im},m} + \zeta'' \varepsilon_{\text{im},m} + \lambda \mathbf{L} \mathbf{x}^2 \quad (10)$$

where \mathbf{x} is the vector of x_m , $\mathbf{Z}_{\text{exp,re}}$ and $\mathbf{Z}_{\text{exp,im}}$ are the real part and imaginary part vector of measured EIS data, $E_{\text{re},m}$ and $E_{\text{im},m}$ are the residual of the real part and imaginary part of measured EIS data, \mathbf{L} is the qth order differentiation matrix [26], $\beta'/2$ and $\beta''/2$ are the shape parameters of real and imaginary parts of the EIS data. $\zeta'/2$ and $\zeta''/2$ are the reciprocal of scale parameters of real and imaginary parts of the EIS data.

Fig. 4 shows the numerical DRT results of $Z_{\text{sim}} + \text{error}$ with or without hyper- ϵ ($\beta' = \beta'' = 2$, $\zeta' = \zeta'' = 10$). From the Nyquist plots in Fig. 4(a), the plots obtained by the above different methods are in good agreement with the Z_{sim} . However, from Fig. 4(b), the frequency deviation caused by erroneous point can be almost completely corrected, and

the area imbalance of DRT peaks is greatly improved by the hyper- ϵ method. Moreover, the pseudo-peak is also suppressed. Table 3 shows the fitting accuracy of numerical DRT with or without hyper- ϵ . By using the hyper- ϵ , the frequency residuals of characteristic peaks P1 and P2 of numerical DRT are reduced from 20.7% and 20.6% to 6.4% and 4%, respectively, the area residual of characteristic peaks P1 and P2 are also reduced from 52.6% and 57.46% to 3.85% and 3.2%, respectively. To demonstrate the ability of the hyper- ϵ method in detecting outliers, the weights are normalized. The normalized weights are $\varepsilon_{\text{re}}/\varepsilon_{\text{re},\text{max}}$ and $\varepsilon_{\text{im}}/\varepsilon_{\text{im},\text{max}}$ where $\varepsilon_{\text{re},\text{max}}$ is the maximum of ε_{re} and $\varepsilon_{\text{im},\text{max}}$ is the maximum of ε_{im} . Fig. 4(c) and (d) shows the normalized weights $\varepsilon_{\text{re}}/\varepsilon_{\text{re},\text{max}}$ and $\varepsilon_{\text{im}}/\varepsilon_{\text{im},\text{max}}$ of the EIS data obtained by the hyper- ϵ . From Fig. 4(d), the imaginary part residual at 3 Hz is given very low weight value. It can be confirmed from the above Nyquist plot in Fig. 3(a) that the introduced

Table 4The fitting accuracy of numerical DRT with or without hyper- ε ($Z_{\text{sim}} + \text{noise}$).

Parameters		Z_{sim}	$Z_{\text{sim}} + \text{noise}$	$Z_{\text{sim}} + \text{noise}$ hy- ε
P1	Characteristic frequency (Hz)	Value	9.9747	9.139
		Residual	0.253%	8.61% 6%
	Time constant (s)	Value	0.1003	0.109
		Residual	0.3%	9% 6.4%
P2	Peak area (mΩ)	Value	100.001	129
		Residual	0.001%	29% 11.16%
	Characteristic frequency (Hz)	Value	5.022	4.294
		Residual	0.44%	14.12% 9%
P3	Time constant (s)	Value	0.1991	0.233
		Residual	0.45%	16.5% 3.8%
	Peak area (mΩ)	Value	99.9998	71.43
		Residual	0.0002%	28.57% 11%
P3	Characteristic frequency (Hz)	Value	\	0.001
		Residual	\	\
	Time constant (s)	Value	\	999.77
		Residual	\	\
P3	Peak area (mΩ)	Value	\	7.542
		Residual	\	\

error point is indeed in the imaginary part of 3 Hz. At the same time, the lower weight can reduce the influence of the error point on the fitting result, thus improving the robustness of numerical DRT.

To analyze the influence of noise data on the numerical DRT, the white noise is added to Z_{sim} , and the synthesis formula is as follows:

$$Z_{\text{sim}} + \text{noise} = Z_{\text{sim}} + \varepsilon |Z_{\text{sim}}| (E' + iE'') \quad (11)$$

where E' and $E'' \sim \text{Normal distribution } N(0, 1)$, ε is the noise level. $\varepsilon = 0.5\%$ in this work, $|Z_{\text{sim}}|$ is the magnitude of the impedance.

The synthesized data $Z_{\text{sim}} + \text{noise}$ is shown in Fig. 5(a). From Fig. 5(b), the noise data results in area imbalance, characteristic frequency deviation, and pseudo-peak appears at the low frequency of numerical DRT peaks. The area imbalance of DRT peaks is improved by the hyper- ε . At the same time the additional pseudo-peak is also suppressed. The normalized weights $\varepsilon_{\text{re}}/\varepsilon_{\text{re,max}}$ and $\varepsilon_{\text{im}}/\varepsilon_{\text{im,max}}$ of the EIS data obtained by the hyper- ω are shown in Fig. 5(c) and (d). Affected by statistical noise, the normalized weights of the real and imaginary residuals vary with the magnitude of the noise.

Table 4 shows the comparison of fitting accuracy of numerical DRT with or without the hyper- ε for $Z_{\text{sim}} + \text{noise}$. By using the hyper- ε , the frequency residuals of characteristic peaks P1 and P2 of numerical DRT are reduced from 8.6% and 14.1% to 6% and 9%, respectively, the area residual of characteristic peaks P1 and P2 are also reduced from 29% and 28.6% to 11.16% and 11%, respectively. From the Fig. S3 in supporting information, the additional pseudo-peak caused by erroneous point is also suppressed but the deviation of characteristic frequency and the imbalance of peak area cannot be improved with the increase of λ .

4. Results and discussion

This section focuses on the application of the improved numerical DRT on PEMFC.

As described in the previous section, the quality of the EIS data is critical for numerical DRT. In addition to the characteristic frequency resolution and regularization parameters to be considered by the algorithm itself, the measured EIS data conforms to the principle of causal, linearity, and time-invariance. The Kramers-Kronig (KK) transformation is a useful verification method for the EIS data that is widely used [45, 46]. In this paper, Lin-KK Tools software [19] is used to verify the measured EIS data. Before analyzing the measured EIS data of PEMFC by numerical DRT, KK validation is required first. The KK-residuals were less than 1% in the whole frequency range (Fig. S5 in supporting information), indicating sufficient quality of the EIS data [39].

As a high-quality EIS data of a PEMFC under 60 °C and 200 mA cm⁻²,

the numerical DRT results with different $\Delta \log f$ at $\lambda = 1e-12$ are shown in Fig. 6. The fitted Nyquist plots change little and fit well with the measured EIS data point gradually with the increase of $\Delta \log f$ in Fig. 6(a). The residuals in Fig. 6(c) and (d) also demonstrate the same results. $\Delta \log f$ has a much more significant effect on numerical DRT in Fig. 6(b), with the increase of $\Delta \log f$, the peaks of numerical DRT become flat gradually. When $\Delta \log f$ increases to 0.2, the number of DRT peaks degenerates from 4 to 3. Detail information is shown in Fig. 6(e), due to the large $\Delta \log f$, there are only two RBFs between the minimum frequency interval $\Delta \log f_{\text{P,min}}$ of P1 and P2, which makes it difficult to extract the characteristic information of P1 and P2. With the decrease of $\Delta \log f$, the two peaks gradually separate completely from Fig. 6(f)–(h). Table 5 shows the fitting results of numerical DRT with different $\Delta \log f$. Therefore, to obtain better numerical DRT fitting results, $\Delta \log f$ is set to be 0.02.

The influence of erroneous point added into EIS data of PEMFC on numerical DRT has been analyzed. The erroneous data results in the area imbalance of P1 and P2 and can be improved by using the hyper- ε method (Fig. S4 in supporting information).

To verify whether the results of the improved numerical DRT can correspond to the theoretical polarization process of PEMFC, the resistance model of charge transfer of PEMFC is established. The main equations are shown below [47,48]:

$$\eta_{\text{act},0.9V}^{\text{therm}} = \frac{2.303RT}{\alpha_c F} \log(i + i_{\text{cross}}) - \frac{2.303RT}{\alpha_c F} \log(i_{0.9V}^{\text{therm}}) + 0.85 \times 10^{-3}(T - 298.15) \quad (12)$$

where $\eta_{\text{act},0.9V}^{\text{therm}}$ is the activation overpotential. R is the ideal gas constant, 8.314 J mol⁻¹K⁻¹. F is the Faraday constant, 96485 C mol⁻¹ T is the cell temperature, °C. α_c is the cathode transfer coefficient. i is the load current density, mA cm⁻². i_{cross} is the current density reference to hydrogen crossover and internal short circuit, mA cm⁻². $i_{0.9V}^{\text{therm}}$ is the exchange current density refers to the iR-free voltage of 0.9 V, mA cm⁻².

The inverse slope of overpotential also represents a kind of polarization resistance [21]. So, the charge transfer resistance R_{ct} can be written as:

$$R_{\text{ct}} = -\frac{\partial \eta_{\text{act},0.9V}^{\text{therm}}}{\partial i} \quad (13)$$

The Nyquist curve of EIS data at various current densities is plotted in Fig. 7(a). The corresponding solid lines are the results of DRT fitting, and the DRT plots are shown in Fig. 7(b). During the low current density range within 200 mA cm⁻², the P1 dominates the distribution and decreases rapidly with current density increases. A strong relationship with the lower current density suggests that P1 is closely correlated with charge transfer process. For large current density ranges above 800 mA cm⁻², the mass transport process dominates the polarization and charge transfer process slightly decreases with current density increases [11]. So, the P1 shifts to the second peak on the left. Fig. 7(c) shows the comparison of the P1 area R_{P1} with R_{ct} . The R_{P1} and the R_{ct} are highly consistent. And the characteristic parameters of the process can be calculated by P1 peak, which verifies that the above improved numerical DRT method can be used to interpret and calculate the polarization processes of PEMFC. However, there are slight differences between R_{P1} and R_{ct} , especially at low current density. The main reasons may lie in two aspects:

- (1) The overpotential $\eta_{\text{act},0.9V}^{\text{therm}}$ in the model is obtained under the condition of 100% RH, but the actual operation condition is difficult to achieve due to the large gases stoichiometries. Therefore, the actual overpotential is larger than $\eta_{\text{act},0.9V}^{\text{therm}}$ [49,50].
- (2) The theoretical model does not consider the increase in the overpotential caused by the Pt oxide-coverage during the reaction [51].

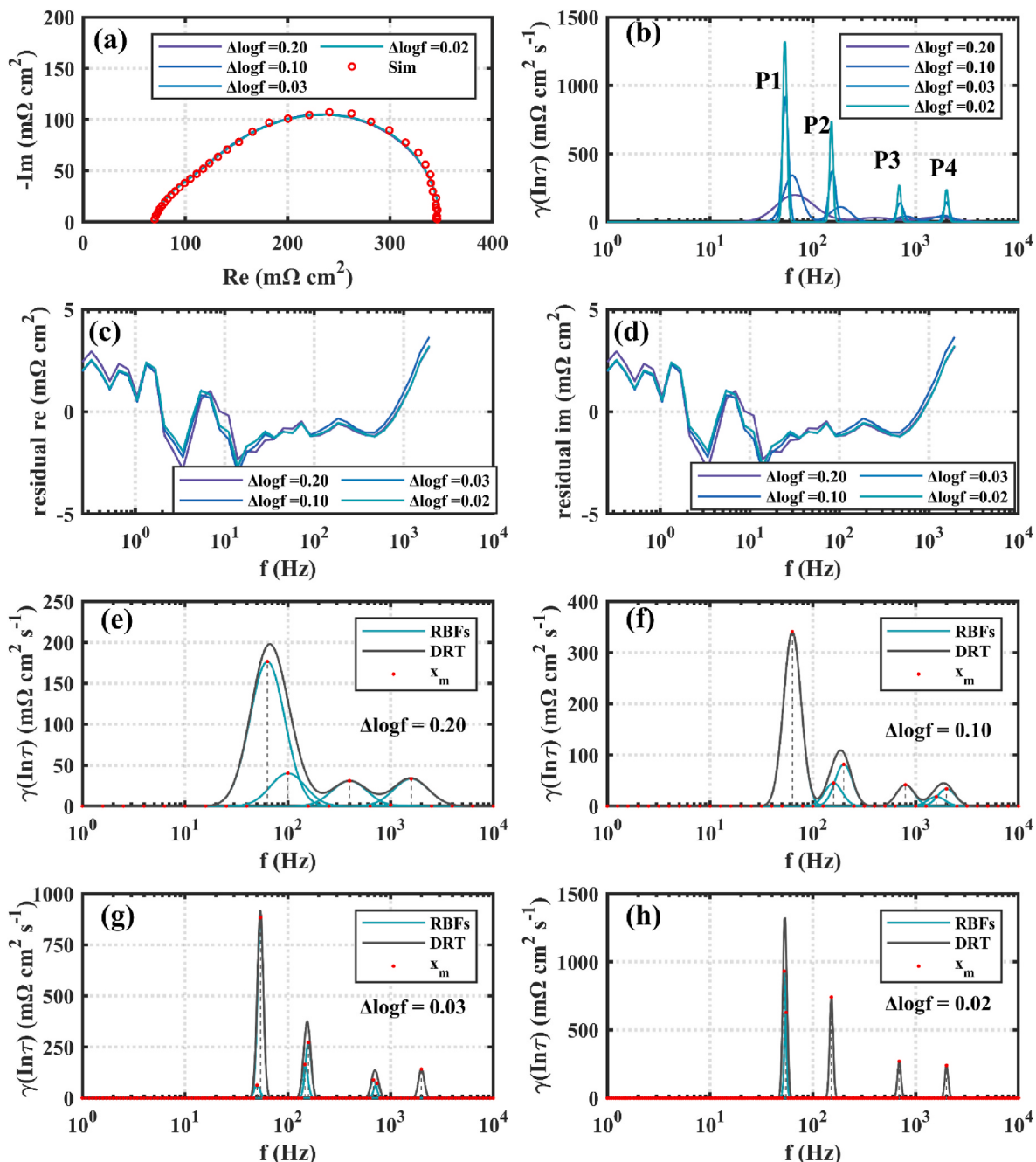


Fig. 6. The numerical DRT results of measured EIS data of 60 °C and 200 mA cm⁻² with different $\Delta\log f$, (a) Nyquist plots, (b) DRT plots, (c) residual of real part vs. frequency, (d) residual of imaginary part vs. frequency, (e) RBFs and x_m of $\Delta\log f = 0.20$, (f) RBFs and x_m of $\Delta\log f = 0.10$, (g) RBFs and x_m of $\Delta\log f = 0.03$, (h) RBFs and x_m of $\Delta\log f = 0.02$.

So, it is determined that the P1 peak is related to the charge transfer process.

From the above analysis, the characteristic frequencies of the polarization processes can be identified by the improved numerical DRT. Then, the characteristic frequency range of the electrochemical system can be obtained, especially the minimum characteristic frequency which can guide the frequency range selection of EIS measurement. This approach can reduce unnecessary low frequency measurement time and enable fast EIS measurement.

The above EIS data of PEMFC at 60 °C and 200 mA cm⁻² is selected to validate the fast EIS measurement approach. The minimum characteristic frequency of the EIS data of 60 °C and 200 mA cm⁻² is about 53 Hz from Table 5. (Indeed, the actual characteristic frequency should be

$53/2\pi = 8.44$ Hz, because the former characteristic frequency is radian frequency which is easy to calculate.) According to the above principles of fast EIS measurement, the minimum frequency selected for EIS measurement is 10 Hz. So, the EIS data from 10 to 2000 Hz is intercepted for numerical DRT analysis and prediction. The DRT results are compared with those of the original data as shown in Fig. 8. From the Nyquist plot in Fig. 8(a), the selected EIS data symbolized in red circle occupies only a semicircle region of the original EIS data. The predicted Nyquist plot obtained by the numerical DRT with selected EIS data fits well with the original data except for some deviations in the low frequency region. The Bode plots in Fig. 8(c)–(f) and the residuals in Fig. 8(g) and (h) also demonstrate more detailed information about the results. From the DRT plot in Fig. 8(b), the characteristic frequency shifts a

Table 5

The numerical DRT results of above measured EIS data with different $\Delta \log f$.

Parameters	$\Delta \log f = 0.02$	$\Delta \log f = 0.03$	$\Delta \log f = 0.1$	$\Delta \log f = 0.2$
P1	Characteristic frequency (Hz)	53.34	54	62.44
	Time constant (s)	0.0187	0.0185	0.016
	Peak area ($\text{m}\Omega$)	152.85	154.57	167.76
P2	Characteristic frequency (Hz)	151	154.4	184.6
	Time constant (s)	0.0066	0.0065	0.0054
	Peak area ($\text{m}\Omega$)	72.64	71.425	61.57
P3	Characteristic frequency (Hz)	691	701	789.46
	Peak time constant (s)	0.0014	0.0014	0.0013
	Peak area ($\text{m}\Omega$)	26.7	26.43	20.5
P4	Characteristic frequency (Hz)	1993	1992	1853
	Time constant (s)	5e-4	5e-4	5.4e-4
	Peak area ($\text{m}\Omega$)	23.5	23.32	25.46
				33.7

little bit to the left, and the peak size of P1 and P2 is also some imbalances in proportion compared to the DRT peaks of original data. The deviations between the predicted impedance and the original impedance at low frequency (>0.1 Hz) is mainly caused by the effect of ultra-low frequency pseudo-inductive [45]. However, the impact is relatively small. The comparison of DRT analysis results under original data and selected data based on characteristic frequency selection from 200 to 1500 mA cm^{-2} is shown in Fig. S6. Meanwhile, the deviations are all within 10% in large current density range, and the shortening of measurement time is huge. The time for measuring the original EIS data from 10 kHz to 0.1 Hz with 11 ppd is about 6 min under the condition of sampling 10 cycles at each frequency point. The selected EIS data with frequency range from 2000 to 10 Hz with 11 ppd under the same condition can shorten the time of this EIS measurement to 5 s.

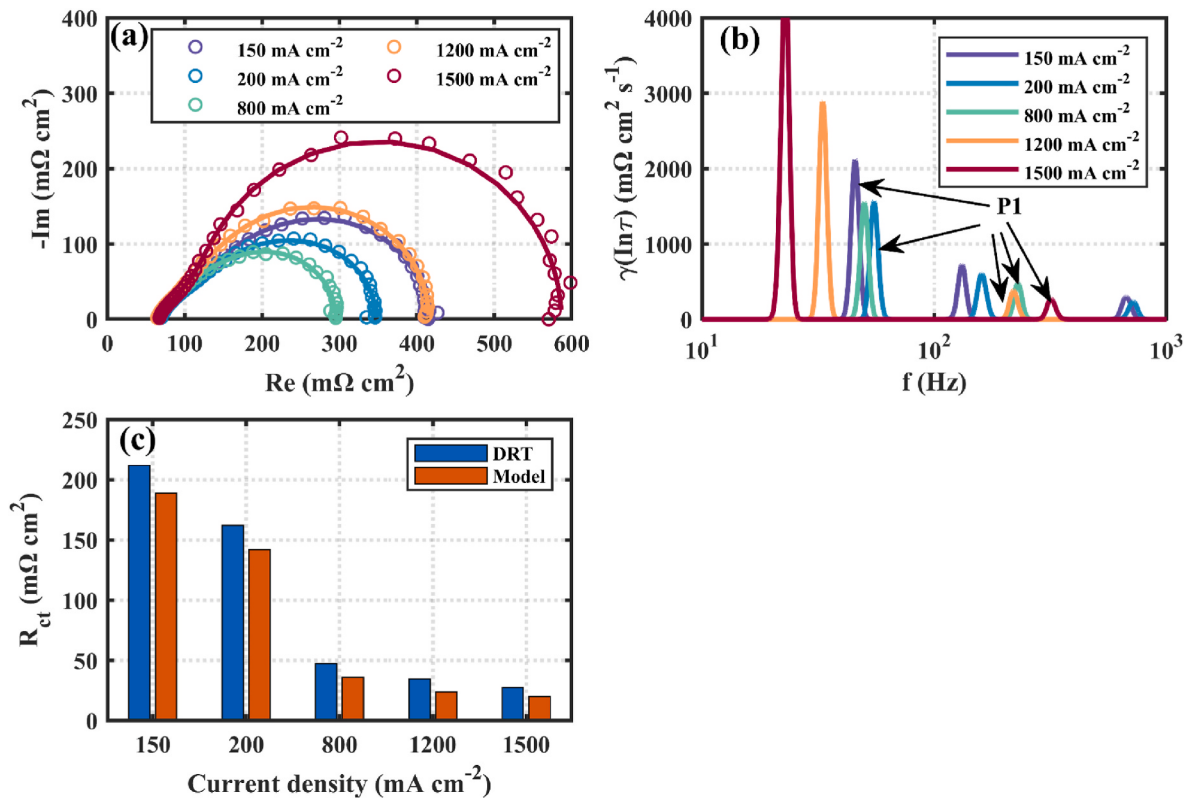
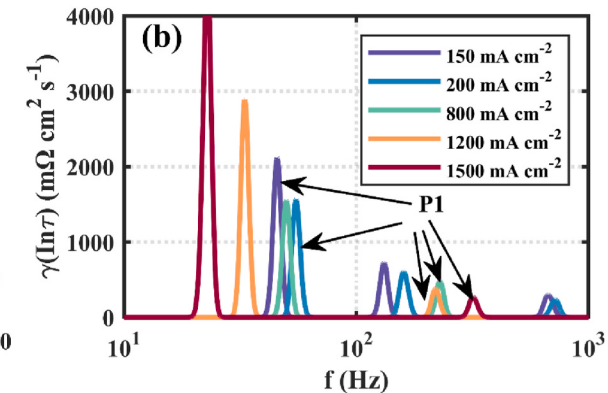


Fig. 7. The comparison of the R_{p1} and the R_{ct} from 150 mA cm^{-2} to 1500 mA cm^{-2} , (a) (a) Nyquist plots, (b) DRT plots, (c) the R_{p1} and the R_{ct} .

5. Conclusion

In this paper, the principle, implementation, and application of the comprehensive regularization DRT based on characteristic frequency resolution and hyperparameters optimization are systematically analyzed. First, the characteristic frequency resolution optimization is applied to avoid peaks overlapping and improve the accuracy of DRT deconvolution. Then, the hyperparameters optimization which assigns weights to each individual data point is applied to overcome the pseudo-peaks and peaks deviation. Moreover, a fast EIS measurement based on characteristic frequency of DRT is proposed and verified by the impedance prediction. The results show that:

- (1) Characteristic frequency resolution has a significant effect on identification accuracy of numerical DRT which represents the minimum logarithmic interval to distinguish two adjacent relaxation times. Characteristic frequency resolution optimization can avoid the peaks overlapping and improve the accuracy of DRT deconvolution.
- (2) This hyperparameters optimization can quickly detect outliers in EIS data and correct pseudo-peaks or peaks deviation caused by erroneous points or noise by properly assigning weights to data points. The λ optimization traditionally can suppress the pseudo-peak, but not much improvement on the peaks deviation.
- (3) The resistance obtained from P1 peak is in good agreement with the theoretical charge transfer kinetic model of PEMFC which demonstrates excellent identification of polarization processes by the improved regularization DRT.
- (4) The fast EIS measurement based on characteristic frequency range obtained by the comprehensive regularization DRT method can greatly shorten the EIS measurement time under the premise of ensuring the impedance identification accuracy. The fast EIS measurement is verified by the EIS data of PEMFC under 200 mA cm^{-2} .



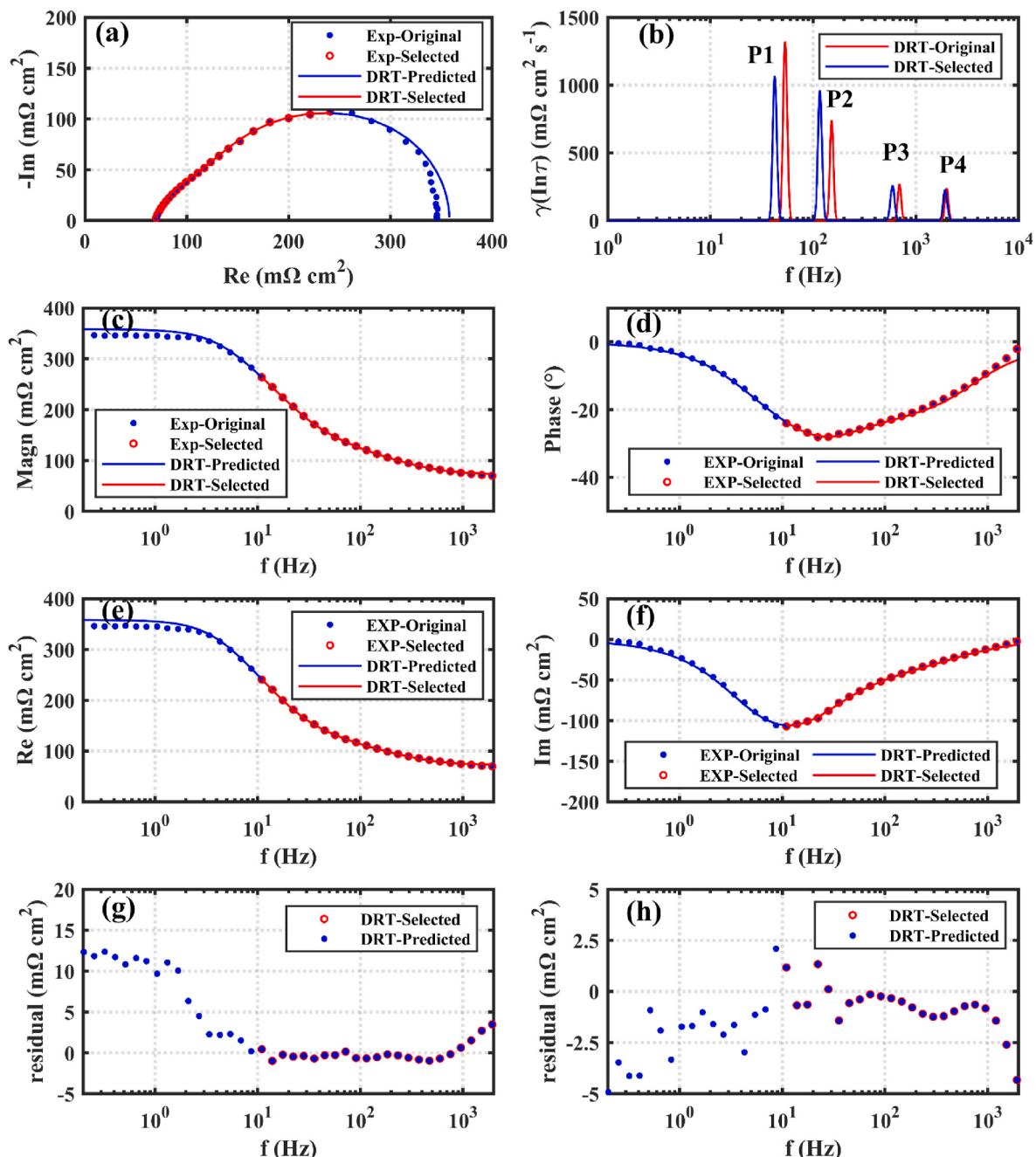


Fig. 8. The numerical DRT analysis and prediction results of measured EIS data of 60 °C and 200 mA cm⁻² with selected frequency range from 10 Hz to 2000 Hz, (a) Nyquist plots, (b) DRT plots, (c) magnitude vs. frequency, (d) phase vs. frequency, (e) real part vs. frequency, (f) imaginary part vs. frequency, (g) residual of real part vs. frequency, (h) residual of imaginary part vs. frequency.

Moreover, this improved regularization DRT and fast EIS measurement method can apply to fault diagnosis, especially on-board applications of PEMFC.

CRediT authorship contribution statement

Dong Zhu: Conceptualization, Methodology, Software, Writing – original draft, Validation. **Tiancai Ma:** Data curation, Writing – review & editing, Supervision, Funding acquisition, Project administration. **Yanbo Yang:** Data curation, Writing – review & editing, Supervision, Funding acquisition.

Declaration of competing interest

The authors declare that they have no known competing financial interests or personal relationships that could have appeared to influence the work reported in this paper.

Data availability

The authors do not have permission to share data.

Acknowledgments

This work has been funded by the National Natural Science

Foundation of China (No. 52077157) and the National Natural Science Foundation of China (No. 52102427).

Appendix A. Supplementary data

Supplementary data to this article can be found online at <https://doi.org/10.1016/j.jpowsour.2022.231955>.

References

- [1] A. Leonide, Y. Apel, E. Ivers-Tiffée, SOFC modeling and parameter identification by means of impedance spectroscopy, *ECS Trans.* 19 (2009) 81–109, <https://doi.org/10.1149/1.3247567>.
- [2] S.M. Rezaei Niya, M. Hoofar, Study of proton exchange membrane fuel cells using electrochemical impedance spectroscopy technique – a review, *J. Power Sources* 240 (2013) 281–293, <https://doi.org/10.1016/j.jpowsour.2013.04.011>.
- [3] Z. Tang, Q.-A. Huang, Y.-J. Wang, F. Zhang, W. Li, A. Li, L. Zhang, J. Zhang, Recent progress in the use of electrochemical impedance spectroscopy for the measurement, monitoring, diagnosis and optimization of proton exchange membrane fuel cell performance, *J. Power Sources* 468 (2020), 228361, <https://doi.org/10.1016/j.jpowsour.2020.228361>.
- [4] T. Ma, W. Lin, Z. Zhang, J. Kang, Y. Yang, Research on electrochemical impedance spectroscopic behavior of fuel cell stack under different reactant relative humidity, *Int. J. Hydrogen Energy* 46 (2021) 17388–17396, <https://doi.org/10.1016/j.ijhydene.2021.02.156>.
- [5] F. Fabregat-Santiago, J. Bisquert, G. Garcia-Belmonte, G. Boschloo, A. Hagfeldt, Influence of electrolyte in transport and recombination in dye-sensitized solar cells studied by impedance spectroscopy, *Sol. Energy Mater. Sol. Cells* 87 (2005) 117–131, <https://doi.org/10.1016/j.solmat.2004.07.017>.
- [6] Q. Wang, J.-E. Moser, M. Grätzel, Electrochemical impedance spectroscopic analysis of dye-sensitized solar cells, *J. Phys. Chem. B* 109 (2005) 14945–14953, <https://doi.org/10.1021/jp052768h>.
- [7] T. Osaka, D. Mukoyama, H. Nara, Review—development of diagnostic process for commercially available batteries, especially lithium ion battery, by electrochemical impedance spectroscopy, *J. Electrochem. Soc.* 162 (2015) A2529–A2537, <https://doi.org/10.1149/2.0141514jes>.
- [8] U. Tröltzsch, O. Kanoun, H.-R. Tränkler, Characterizing aging effects of lithium ion batteries by impedance spectroscopy, *Electrochim. Acta* 51 (2006) 1664–1672, <https://doi.org/10.1016/j.electacta.2005.02.148>.
- [9] D.J. Xiong, L.D. Ellis, R. Petibon, T. Hynes, Q.Q. Liu, J.R. Dahn, Studies of gas generation, gas consumption and impedance growth in Li-ion cells with carbonate or fluorinated electrolytes using the pouch bag method, *J. Electrochem. Soc.* 164 (2016) A340–A347, <https://doi.org/10.1149/2.1091702jes>.
- [10] Y. Abd-elrhman, M.A.H. Gepreel, A. Abdel-Moniem, S. Kobayashi, Compatibility assessment of new V-free low-cost Ti-4.7Mo-4.5Fe alloy for some biomedical applications, *Mater. Des.* 97 (2016) 445–453, <https://doi.org/10.1016/j.matdes.2016.02.110>.
- [11] H. Yuan, H. Dai, P. Ming, X. Wang, X. Wei, Quantitative analysis of internal polarization dynamics for polymer electrolyte membrane fuel cell by distribution of relaxation times of impedance, *Appl. Energy* 303 (2021), <https://doi.org/10.1016/j.apenergy.2021.117640>.
- [12] J. Huang, Z. Li, B.Y. Liaw, J. Zhang, Graphical analysis of electrochemical impedance spectroscopy data in Bode and Nyquist representations, *J. Power Sources* 309 (2016) 82–98, <https://doi.org/10.1016/j.jpowsour.2016.01.073>.
- [13] A.M. Dhirde, N.V. Dale, H. Salehfari, M.D. Mann, T. Han, Equivalent electric circuit modeling and performance analysis of a PEM fuel cell stack using impedance spectroscopy, *IEEE Trans. Energy Convers.* 25 (2010) 778–786, <https://doi.org/10.1109/TEC.2010.2049267>.
- [14] D.D. Macdonald, Reflections on the history of electrochemical impedance spectroscopy, *Electrochim. Acta* 51 (2006) 1376–1388, <https://doi.org/10.1016/j.electacta.2005.02.107>.
- [15] P.M. Ramos, F.M. Janeiro, Gene expression programming for automatic circuit model identification in impedance spectroscopy: performance evaluation, *Measurement* 46 (2013) 4379–4387, <https://doi.org/10.1016/j.measurement.2013.05.011>.
- [16] T. Ma, Z. Zhang, W. Lin, M. Cong, Y. Yang, Impedance prediction model based on convolutional neural networks methodology for proton exchange membrane fuel cell, *Int. J. Hydrogen Energy* 46 (2021) 18534–18545, <https://doi.org/10.1016/j.ijhydene.2021.02.204>.
- [17] J. Ross Macdonald, Three to six ambiguities in immittance spectroscopy data fitting, *J. Phys. Condens. Matter* 24 (2012), 175004, <https://doi.org/10.1088/0953-8984/24/17/175004>.
- [18] M. Saccoccia, T.H. Wan, C. Chen, F. Ciucci, Optimal regularization in distribution of relaxation times applied to electrochemical impedance spectroscopy: ridge and lasso regression methods - a theoretical and experimental study, *Electrochim. Acta* 147 (2014) 470–482, <https://doi.org/10.1016/j.electacta.2014.09.058>.
- [19] Y. Zhang, Y. Chen, M. Li, M. Yan, M. Ni, C. Xia, A high-precision approach to reconstruct distribution of relaxation times from electrochemical impedance spectroscopy, *J. Power Sources* 308 (2016) 1–6, <https://doi.org/10.1016/j.jpowsour.2016.01.067>.
- [20] T.H. Wan, M. Saccoccia, C. Chen, F. Ciucci, Influence of the discretization methods on the distribution of relaxation times deconvolution: implementing radial basis functions with DRTtools, *Electrochim. Acta* 184 (2015) 483–499, <https://doi.org/10.1016/j.electacta.2015.09.097>.
- [21] E. Tuncer, S.M. Gubanski, On dielectric data analysis - using the Monte Carlo method to obtain relaxation time distribution and comparing non-linear spectral function fits, *IEEE Trans. Dielectr. Electr. Insul.* 8 (2001) 310–320, <https://doi.org/10.1109/94.933337>.
- [22] B.A. Boukamp, Fourier transform distribution function of relaxation times; application and limitations, *Electrochim. Acta* 154 (2015) 35–46, <https://doi.org/10.1016/j.electacta.2014.12.059>.
- [23] T. Horlin, Deconvolution and maximum entropy in impedance spectroscopy of noninductive systems, *Solid State Ionics* 107 (1998) 241–253, [https://doi.org/10.1016/S0167-2738\(98\)00008-3](https://doi.org/10.1016/S0167-2738(98)00008-3).
- [24] T. Ivers, E.E. Acacute, A. Weber, eacute, Evaluation of electrochemical impedance spectra by the distribution of relaxation times, *J. Ceram. Soc. Jpn.* 125 (2017) 193–201, <https://doi.org/10.2109/jcersj2.16267>.
- [25] K. Kobayashi, T.S. Suzuki, Distribution of relaxation time analysis for non-ideal immittance spectrum: discussion and progress, *J. Phys. Soc. Jpn.* 87 (2018), 094002, <https://doi.org/10.7566/JPSJ.87.094002>.
- [26] M.B. Effat, F. Ciucci, Bayesian and hierarchical bayesian based regularization for deconvolving the distribution of relaxation times from electrochemical impedance spectroscopy data, *Electrochim. Acta* 247 (2017) 1117–1129, <https://doi.org/10.1016/j.electacta.2017.07.050>.
- [27] A. Leonide, V. Sonn, A. Weber, E. Ivers-Tiffée, Evaluation and modelling of the cell resistance in anode supported solid oxide fuel cells, *ECS Trans.* 7 (2019) 521–531, <https://doi.org/10.1149/1.2729132>.
- [28] D. Guo, G. Yang, G. Zhao, M. Yi, X. Feng, X. Han, L. Lu, M. Ouyang, Determination of the differential capacity of lithium-ion batteries by the deconvolution of electrochemical impedance spectra, *Energies* 13 (2020) 915, <https://doi.org/10.3390/en13040915>.
- [29] X. Zhou, J. Huang, Z. Pan, M. Ouyang, Impedance characterization of lithium-ion batteries aging under high-temperature cycling: importance of electrolyte-phase diffusion, *J. Power Sources* 426 (2019) 216–222, <https://doi.org/10.1016/j.jpowsour.2019.04.040>.
- [30] M. Heinmann, A. Weber, E. Ivers-Tiffée, Advanced impedance study of polymer electrolyte membrane single cells by means of distribution of relaxation times, *J. Power Sources* 402 (2018) 24–33, <https://doi.org/10.1016/j.jpowsour.2018.09.004>.
- [31] A. Weiß, S. Schindler, S. Galbiati, M.A. Danzer, R. Zeis, Distribution of relaxation times analysis of high-temperature PEM fuel cell impedance spectra, *Electrochim. Acta* 230 (2017) 391–398, <https://doi.org/10.1016/j.electacta.2017.02.011>.
- [32] S. Dierickx, A. Weber, E. Ivers-Tiffée, How the distribution of relaxation times enhances complex equivalent circuit models for fuel cells, *Electrochim. Acta* 355 (2020), <https://doi.org/10.1016/j.electacta.2020.136764>.
- [33] F. Ciucci, C. Chen, Analysis of electrochemical impedance spectroscopy data using the distribution of relaxation times: a bayesian and hierarchical bayesian approach, *Electrochim. Acta* 167 (2015) 439–454, <https://doi.org/10.1016/j.electacta.2015.03.123>.
- [34] A. Debenjak, J. Petrovcić, P. Boskoski, B. Musizza, D. Juricic, Fuel cell condition monitoring system based on interconnected DC–DC converter and voltage monitor, *IEEE Trans. Ind. Electron.* 62 (2015) 5293–5305, <https://doi.org/10.1109/tie.2015.2434792>.
- [35] H. Lu, J. Chen, C. Yan, H. Liu, On-line fault diagnosis for proton exchange membrane fuel cells based on a fast electrochemical impedance spectroscopy measurement, *J. Power Sources* 430 (2019) 233–243, <https://doi.org/10.1016/j.jpowsour.2019.05.028>.
- [36] N. Katayama, S. Kogoshi, Real-time electrochemical impedance diagnosis for fuel cells using a DC–DC converter, *IEEE Trans. Energy Convers.* 30 (2015) 707–713, <https://doi.org/10.1109/TEC.2014.2376529>.
- [37] L. Das, B. Srinivasan, R. Rengaswamy, On-line performance monitoring of PEM fuel cell using a fast EIS approach, in: 2015 American Control Conference (ACC), 2015, pp. 1611–1616, <https://doi.org/10.1109/ACC.2015.7170963>.
- [38] X. Yuan, J.C. Sun, M. Blanco, H. Wang, J. Zhang, D.P. Wilkinson, AC impedance diagnosis of a 500W PEM fuel cell stack: Part I: stack impedance, *J. Power Sources* 161 (2006) 920–928, <https://doi.org/10.1016/j.jpowsour.2006.05.003>.
- [39] B.A. Boukamp, Derivation of a distribution function of relaxation times for the (fractal) finite length Warburg, *Electrochim. Acta* 252 (2017) 154–163, <https://doi.org/10.1016/j.electacta.2017.08.154>.
- [40] B.A. Boukamp, A. Rolle, Analysis and application of distribution of relaxation times in solid state ionics, *Solid State Ionics* 302 (2017) 12–18, <https://doi.org/10.1016/j.ssi.2016.10.009>.
- [41] M.E. Ozarem, P. Shukla, M.A. Membrino, Extension of the measurement model approach for deconvolution of underlying distributions for impedance measurements, *Electrochim. Acta* 47 (2002) 2027–2034, [https://doi.org/10.1016/S0013-4686\(02\)00065-8](https://doi.org/10.1016/S0013-4686(02)00065-8).
- [42] D. Klotz, A. Weber, E. Ivers-Tiffée, Practical guidelines for reliable electrochemical characterization of solid oxide fuel cells, *Electrochim. Acta* 227 (2017) 110–126, <https://doi.org/10.1016/j.electacta.2016.12.148>.
- [43] N. Schlüter, S. Ernst, U. Schröder, Finding the optimal regularization parameter in distribution of relaxation times analysis, *Chemelectrochem* 6 (2019) 6027–6037, <https://doi.org/10.1002/celc.201901863>.
- [44] M.-B. Choi, J. Shin, H.-I. Ji, H. Kim, J.-W. Son, J.-H. Lee, B.-K. Kim, H.-W. Lee, K. J. Yoon, Interpretation of impedance spectra of solid oxide fuel cells: L-curve criterion for determination of regularization parameter in distribution function of relaxation times technique, *J. Occup. Med.* 71 (2019) 3825–3834, <https://doi.org/10.1007/s11837-019-03762-8>.

- [45] B.A. Boukamp, A linear kramig-kramers transform test for immittance data validation, *J. Electrochim. Soc.* 142 (1995) 1885–1894, <https://doi.org/10.1149/1.2044210>.
- [46] M. Schönleber, D. Klotz, E. Ivers-Tiffée, A method for improving the robustness of linear kramers-kramers validity tests, *Electrochim. Acta* 131 (2014) 20–27, <https://doi.org/10.1016/j.electacta.2014.01.034>.
- [47] K.C. Neyerlin, W. Gu, J. Jorne, H.A. Gasteiger, Determination of catalyst unique parameters for the oxygen reduction reaction in a PEMFC, *J. Electrochim. Soc.* 153 (2006) A1955, <https://doi.org/10.1149/1.2266294>.
- [48] D. Zhu, Y. Yang, F. Pei, T. Ma, High-precision identification of polarization processes of distribution of relaxation times by polarization curve model for proton exchange membrane fuel cell, *Energy Convers. Manag.* 268 (2022), 115994, <https://doi.org/10.1016/j.enconman.2022.115994>.
- [49] Y. Liu, M.W. Murphy, D.R. Baker, W. Gu, C. Ji, J. Jorne, H.A. Gasteiger, Proton conduction and oxygen reduction kinetics in PEM fuel cell cathodes: effects of ionomer-to-carbon ratio and relative humidity, *J. Electrochim. Soc.* 156 (2009) B970, <https://doi.org/10.1149/1.3143965>.
- [50] J. Shen, L. Xu, H. Chang, Z. Tu, S.H. Chan, Partial flooding and its effect on the performance of a proton exchange membrane fuel cell, *Energy Convers. Manag.* 207 (2020), 12537, <https://doi.org/10.1016/j.enconman.2020.112537>.
- [51] N.P. Subramanian, T.A. Greszler, J. Zhang, W. Gu, R. Makharia, Pt-oxide coverage-dependent oxygen reduction reaction (ORR) kinetics, *J. Electrochim. Soc.* 159 (2012) B531–B540, <https://doi.org/10.1149/2.088205jes>.